Effect of Nb Alloying Addition on Local Phase Transformation at Microtwin Boundaries in Nickel-Based Superalloys

A. J. Egan, Y. Rao, G. B. Viswanathan, T. M. Smith, M. Ghazisaeidi, S. Tin, and M. J. Mills

Abstract

This work investigates two nominally similar polycrystalline alloys, with a subtle difference in Nb content, intended to elucidate its effect on local phase transformation strengthening during high temperature creep. Tests were conducted at 750 °C and 600 MPa to target the creep regime dominated by superlattice intrinsic and extrinsic stacking faults, as well as microtwinning. Alloy A, with higher Nb and lower Al, was found to be superior in creep strength to Alloy B, with lower Nb and higher Al, as well as previously investigated ME3 and LSHR. Atomic resolution scanning transmission electron microscopy and energy-dispersive spectroscopy found that this increased creep strength was due to a novel local phase transformation occurring along microtwin boundary interfaces as a result of the Nb increase. Complementary density functional theory calculations helped to confirm that this was χ phase formation. It is hypothesized that this transformation was the cause of the increased creep strength exhibited by Alloy A.

Keywords

Local phase transformation • Creep • Microtwin • HAADF • STEM

Introduction

Nickel-based superalloys are the materials of choice for applications where high temperature strength and resistance to harsh environmental conditions are major design requirements [1–3]. These properties make them ideal for use in hot sections of aerospace turbine engines, where they are subjected to gas streams in excess of 1600 °C. As a result, turbine disks reach average service temperatures of 650 °C with stresses reaching 1000 MPa. Superalloys are one of the most important materials used in the aeroengine due to the strong dependence of thrust and fuel economy on their service temperature, i.e., high temperature strength, which currently limits engine efficiency. A modest increase in the operating temperature of these materials by 25 °C can increase efficiency by 1% [4] and is therefore a key driving force for research in this material system. Much of this research is focused on creep, the high temperature deformation with time under constant load, which presents the most potent restriction on material performance at the limit of temperature [5].

Despite improved understanding of factors that control high temperature strength, which has led to a fourfold increase in creep rupture life since 1980 [1], there are still questions concerning the mechanisms by which nickel superalloys accumulate damage and defeat the strengthening γ' ($L1_2$) phase. This is particularly evident in the creep regime dominated by faulting and microtwinning, where deformation appears to be controlled by local segregation events near these features [5–10]. Some of these segregation events seem to be highly dependent on alloy composition and can have profound effects, whether positive or

A. J. Egan (✉) · Y. Rao · G. B. Viswanathan · M. Ghazisaeidi · M. J. Mills
Department of Materials Science and Engineering, The Ohio State University, 177 Watts Hall, 2041 N. College Road, Columbus, OH 43210, USA
e-mail: egan.74@osu.edu

A. J. Egan · G. B. Viswanathan · M. J. Mills
Center for Electron Microscopy and Analysis, The Ohio State University, Columbus, OH 43212, USA

T. M. Smith
NASA Glenn Research Center, 21000 Brookpark Rd, Cleveland, OH 44135, USA

S. Tin
Illinois Institute of Technology, 10 W. 32nd Street, Chicago, IL 60616, USA

S. Tin et al. (eds.), *Superalloys 2020*, The Minerals, Metals & Materials Series,
https://doi.org/10.1007/978-3-030-51834-9_62

deleterious, on creep performance; formation of phases along deformation structures induced by segregation has been attributed to increased creep resistance [5]. This phenomenon has been coined local phase transformation (LPT) strengthening by collaborators at the Ohio State University who discovered this phenomenon, and present work continues to elucidate these effects [10]. Many authors have focused on the roles that Co and Cr play in the formation of these planar features; it is presently clear that these serve to lower the stacking fault energy of highly unfavorable complex stacking faults (CSFs) created by the *a*/6 <112> partials which are associated with the propagation of the faults [5–7, 11–16]. Recent research has focused on elements such as Ta, Ti, Hf, and Nb, which have been found to promote the η ($D0_{24}$) LPT strengthening effect on superlattice extrinsic stacking faults (SESFs). Studies by Smith et al. [5] comparing the creep behavior of ME3 and ME501 have illustrated the significance of these local phase transformations; it was found that ME501 was markedly more resistant to creep than ME3, with all the creep strain in the latter coming from microtwinning, whereas ME501 was devoid of microtwins at the small strain levels examined. Instead, SESFs decorated with an η LPT were observed. This suggested that the formation of η phase prevented deleterious thickening of SESFs into microtwins by restricting partial movement along these features, whereas the γ-like LPT via Co and Cr enrichment promoted a softening effect in ME3. An additional LPT to $D0_{19}$ Co_3(Cr, Mo, W) χ phase has been observed by Smith et al. [8] along superlattice intrinsic stacking faults (SISFs) in both ME501 and CMSX-4, and similar results have also been reported by Titus et al. [17] in the Co-based superalloys. This χ LPT appears to be promoted by Mo and W additions, with recent work comparing creep behavior of LSHR and ME3 confirming it as an effective strengthening effect [10]. It has been proposed that this inhibits the shear of <112> stacking fault ribbons, which pose a γ-like LPT softening similar to microtwin propagation. These LPT effects are summarized in Fig. 1, as well as orientation dependencies investigated previously at OSU [12].

As these LPTs are driven by segregation of solute, bulk composition of the alloys may be important in predicting when strengthening phases precipitate on planar defects. Previous work conducted by Antonov et al. [18] has produced a composition correlation map for bulk η/δ formation. Current collaboration with Sammy Tin at the Illinois Institute of Technology (IIT) has leveraged the OSU concept of LPT strengthening by η formation and provided a composition correlation map adapted from previous work by Antonov et al. [18], Fig. 2, that is helpful in guiding exploration of the η LPT composition regime. The horizontal axis indicates preference for η (and δ) phase formation, while the vertical axis indicates γ' preference; below the dashed, empirically determined line, alloys tend to be unstable to bulk phase formation when processed conventionally. The present research has focused on the remarkably strong LPT alloy (Alloy A) shown in Fig. 2 and is "on the borderline" of instability to deleterious bulk phases. It is suspected that alloys along this borderline are more prone to the formation of strengthening η LPTs, as seen by the relative proximity of ME501 vs ME3.

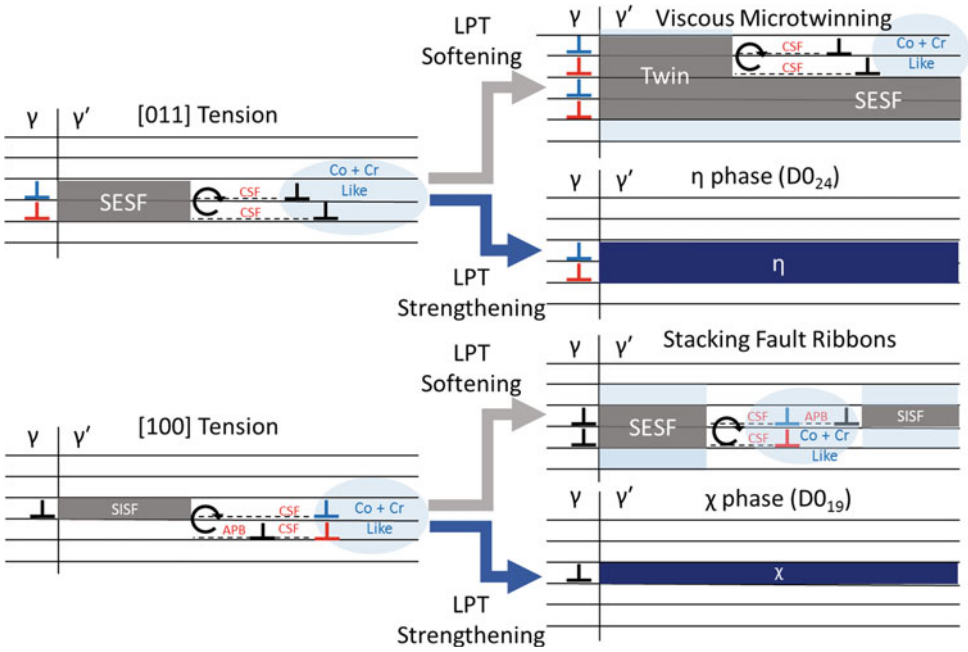

Fig. 1 γ' shearing mechanisms as a function of crystal orientation and the alloy's tendency to form softening/strengthening LPTs

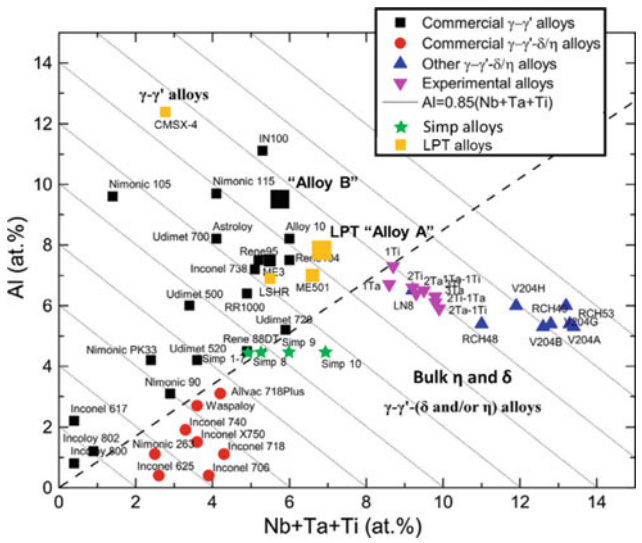

Fig. 2 η/δ composition correlation map. Adapted from Antonov et al. [18] showing relevant alloys in this and previous works. Note the empirically determined dashed line separates stable from unstable microstructures

Of particular interest in the current study were the effects of small compositional differences on deformation due to the segregation events driving strengthening. This was probed by comparing two alloys that are identical in processing history and composition except for a 1 at.% exchange of Nb and Al. The creep strength of these alloys was compared and postmortem deformation examined via scanning transmission electron microscopy (STEM) techniques to determine any differences. In this study, high angle annular dark field (HAADF) STEM has revealed for the first time a new type of LPT strengthening. Investigation of deformation-induced microtwins in Alloy A has shown ordering and chemical signatures along the twin interfaces. Super-X energy-dispersive spectroscopy (EDS) scans of these regions supported this conclusion, which show local increase in Nb content. In addition, density functional theory (DFT) models of segregation driving forces have been utilized to better understand how these complex deformation processes are influenced by surrounding solute.

Materials and Methods

Sample Preparation

Two experimental alloys obtained from IIT that were nominally identical, with the exceptions of Al and Nb, were examined in this study. These alloys were received in the as-forged condition from a hot isostatically pressed (HIP) billet. The compositions of these alloys, A and B, are shown in Table 1 along with relevant alloys for comparison.

Alloys A and B were supersolvus processed at 1170 °C for 1 h and cooled from solution temperature at ~2 °C/s to room temperature followed by aging at 850 °C for 4 h. The resulting microstructures consisted primarily of secondary γ' precipitates with average diameters ranging between 250 and 275 nm. Although some tertiary γ' with an average diameter of 55 nm was heterogeneously distributed within the microstructure, their impact on the overall γ' volume fraction of ~49% was minimal. Creep tests were performed by Westmoreland and were conducted at 750 °C under 600 MPa to rupture following ASTM E139. After failing, the samples were furnace cooled under load.

Deformation Characterization

Postmortem specimens were ground through 1200 grit SiC paper and then polished to a 0.05 μm colloidal silica finish using an Allied Multiprep such that the scanning electron microscope (SEM) view was down the tensile axis. Electron backscattered diffraction (EBSD) was conducted in a Thermo Scientific Apreo SEM to determine suitable grains and orientation of focused ion beam (FIB) TEM foils. Platinum was used to mark foils such that they would produce a foil normal to <110> orientation in order to view planar defects edge-on. These were taken from grains of <110> parallel to the tensile axis to compare deformation characteristics between alloys. Foils were extracted and prepared using a Thermo Scientific Helios Nanolab DualBeam 600 FIB. The foils were nanomilled using a Fischione Model 1040 Nanomill prior to STEM imaging. A Thermo Scientific

Table 1 Composition of Alloys A and B, along with relevant alloys [10]

Alloy	Composition at.%												
	Ni	Co	Cr	Al	Ti	Nb	W	Ta	Mo	Zr	B	c	111
ME3	Bal.	21	14	7.3	4.6	0.5	0.66	0.76	2.2	0 03	0.1	0.2	0
LSHR	Bal.	20.1	13.9	7.5	4.2	0.94	1.4	0.48	1.6	0.032	0.16	0.22	0
Alloy A	Bal.	IS	5.0–16.0	8.0	0	5.5	0–2.0	1	0–3.0	0	0	0	0
Alloy B	Bal.	18 25	5.0–16.0	9.8	0	4.6	0–2.0	1	0–3.0	0	0	0	0

Tecnai F20 field emission 200 kV STEM was used to take HAADF images of overall deformation. These were taken slightly off-zone to allow for multiple diffraction conditions to be active at the same time. Atomic resolution HAADF-STEM images were taken using a Thermo Scientific Titan^3 60–300 S-Twin. The Super-X EDS detector was used for elemental analysis utilizing either Bruker Espirit or Thermo Scientific VELOX software. Signal from EDS line scans was integrated vertically, as marked.

Results

Tensile Creep Behavior

Creep tests were performed to rupture on Alloys A and B at 750 °C and 600 MPa. The creep curves are shown in Fig. 3, along with a comparison to ME3 and LSHR. These latter alloys are known to exhibit detrimental γ and strengthening χ, respectively, LPTs based on prior study [10]. It is evident that Alloy A possessed superior strength, in terms of a lower creep rate, as compared to the other alloys tested. Note that while Alloy A's creep rate was lower, its time to rupture was about 21% shorter than Alloy B. Alloy A's lower creep rate is significant given that ME3 and LSHR were tested at a considerably lower load of 551 MPa.

Deformation Characterization Using STEM

Following creep testing, HAADF STEM was used to examine the postmortem deformation behavior. Figure 4 shows near <110> zone axis images of Alloys A and B.

It is evident in Fig. 4a, b that microtwinning was the dominant deformation mode active in both alloys. While not as clear in Fig. 4a, both alloys exhibit matrix dislocations active and isolated faulting does occur, albeit less frequently. Note that while Alloy B appears to have a higher density of defects, this was likely due to the increased strain (~2%) in this sample and it is hard to draw these comparisons. It would be beneficial to conduct interrupted creep tests on these alloys at the same strain in order to compare the defect density, which is planned for the future study.

Atomic Resolution STEM and Elemental Analysis of Twins

Previous studies have demonstrated that alloys dominated by microtwinning, such as ME3, typically have a γ-like LPT along the twins and significant Cottrell atmospheres of γ-former elements which serve to lower the high stacking fault energy caused by passage of $a/6$ <112> thickening partial dislocations [5–7, 11–16]. For this reason, it was of interest to compare the solute segregation surrounding the microtwins, particularly in Alloy A which had a lower creep rate than previously investigated LSHR. Lower magnification, low camera length HAADF-STEM images show that segregation was indeed present at microtwins in both alloys, and EDS scans confirm the presence of multiple segregating species. Figure 5 presents results for the case of Alloy A. Note the hole present was purposely drilled with the electron beam for drift correction due to the limitations of the Bruker software when performing scans at magnification suitable for viewing atomic structure.

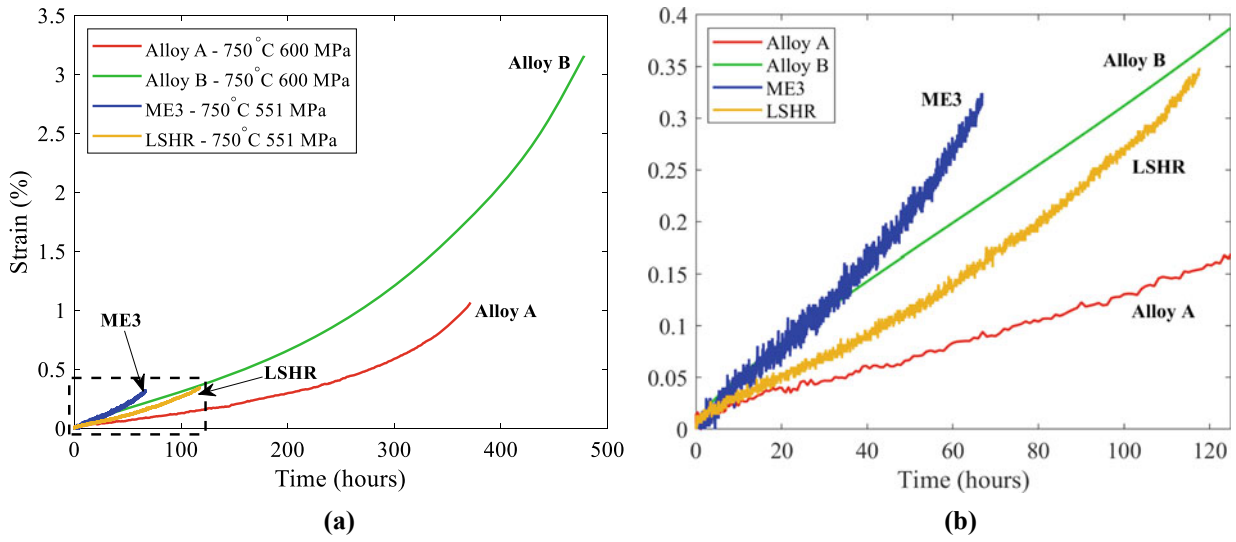

Fig. 3 **a** Creep response of Alloys A and B. **b** Inset comparing creep behavior to other relevant commercial alloys

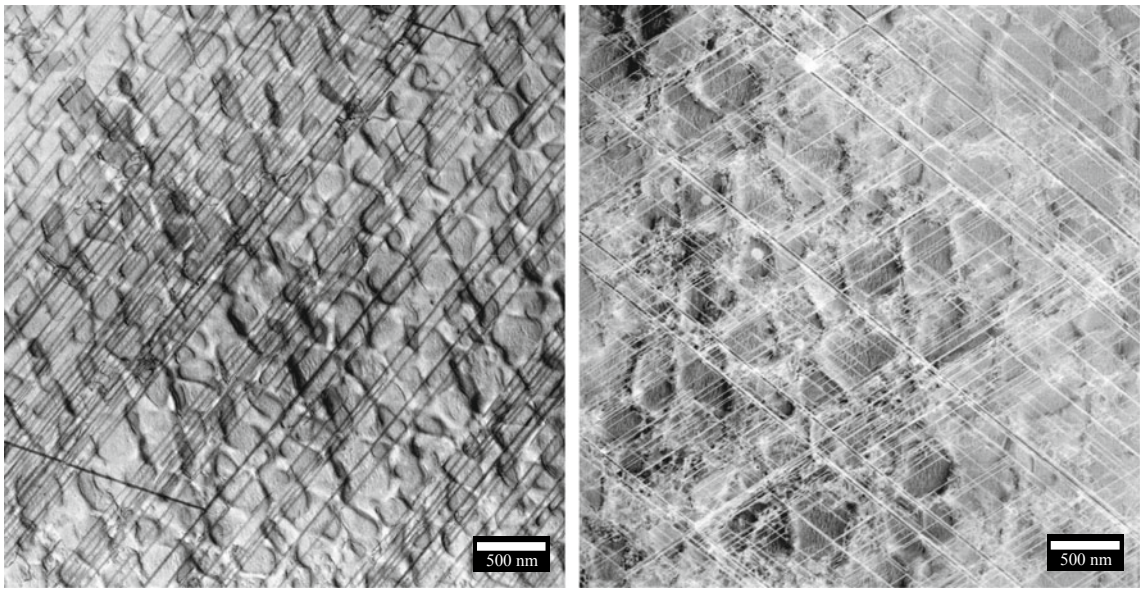

Fig. 4 Near <110> zone axis images showing microtwinning in Alloy A (**a**) and Alloy B (**b**)

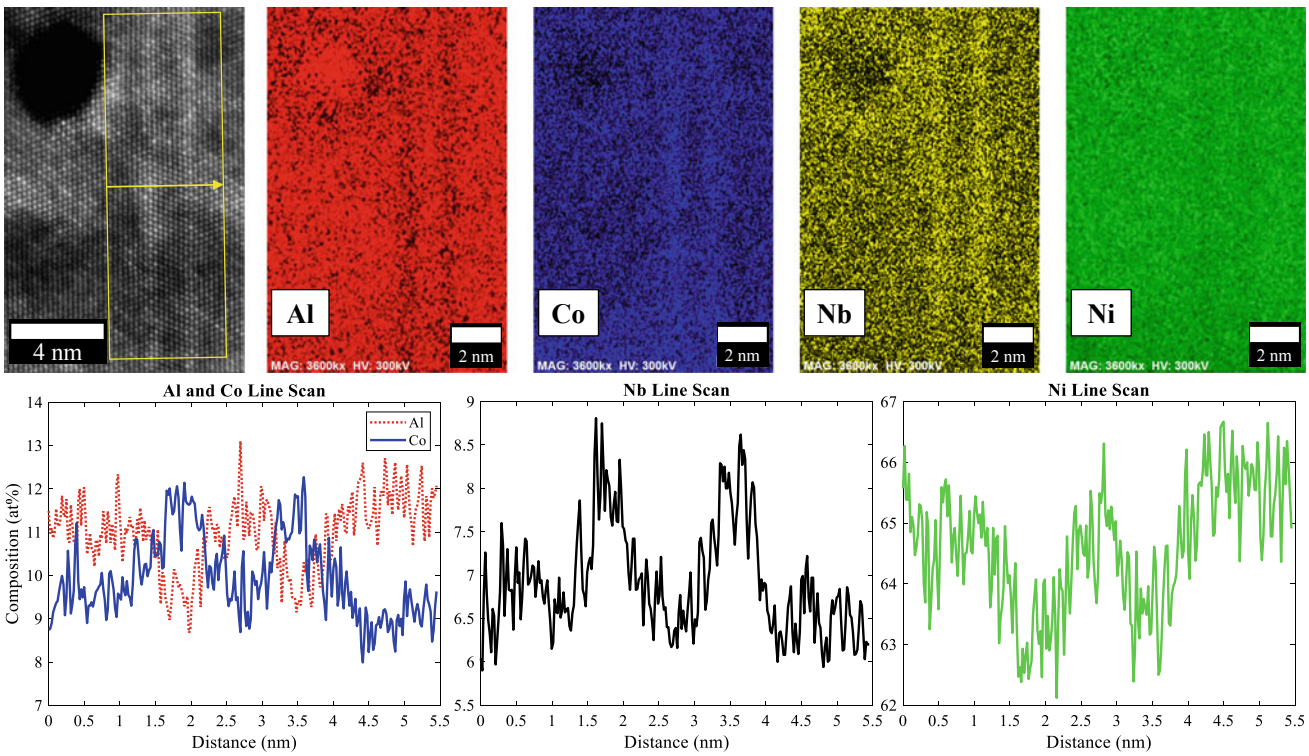

Fig. 5 HAADF image of Alloy A and accompanying EDS maps of segregating species. Vertically integrated EDS line scans across the microtwin as marked

The EDS maps and corresponding vertically integrated line scans show that Alloy A exhibited a decrease in Al and Ni with an enrichment of Co, which is typical for microtwin boundaries based on previous studies [6, 7, 13]. However, this type of segregation alone would lead to darker contrast of the microtwin relative to the bulk γ' due to the replacement of Ni with lower atomic number Co. The microtwin present in Fig. 5 exhibited the opposite contrast. What is of

interest here is the 1.5–1.75 at.% (depending on the peak examined) increase of Nb to the twin interface, which has not been reported previously, and would cause the increased intensity at these interfaces in the HAADF image.

This result is juxtaposed with that for Alloy B, which is shown in Fig. 6. Here, it is noticeable that this microtwin was significantly thicker than the one examined in Alloy A. In terms of the segregation profile, the results were similar, although the decrease of Al and Ni and enrichment of Co were slightly smaller in magnitude. This was also the case for Nb which still increased in concentration versus the γ', but only in the range 0.5–1 at.%. Note that Cr (not shown) content was not found to segregate along the microtwins in either Alloy A or B, which is an unusual characteristic of these alloys as compared to previously examined microtwins [6, 7, 9, 13].

While microtwins in both Alloys A and B exhibited enhanced contrast at the twin boundary, there was a significant difference between the two alloys when examined at high enough magnification to clearly resolve the atomic arrangements across the microtwin interfaces. Examining these defects in both alloys side by side, as shown in Fig. 7 for similar imaging conditions, it is clear that Alloy A exhibits a "zig-zag" ordering along both interfaces of the twin boundary, whereas Alloy B contains bright contrast but is devoid of any apparent ordering. The bright, ordered columns likely correspond to Nb, as revealed in the EDS scans. The lack of ordering in Alloy B is consistent with that found at detrimental microtwins in previous work, such as those examined in ME3 [5, 11].

Analysis of Other Planar Defects

In addition to the aforementioned microtwins, a variety of planar defects were present in both alloys studied. Although this is not the main focus of the discussion, it is important to acknowledge their contribution to the creep behavior in these alloys. Both alloys exhibited the presence of SESFs, which is to be expected given that microtwins are formed via passage of $a/6$ <112> Shockley partials along SESFs and consequent reordering [7, 19–24]. Examples of their appearance in both alloys are shown in Fig. 8a (Alloy A) and Fig. 9 (Alloy B).

Alloy B not only exhibited SESFs, but also SISFs. This was unexpected given that this FIB foil was obtained from a grain with <110> parallel to the tensile axis, whereas SISFs are reported to typically form in grains with <100> parallel to this [12]. However, their presence is relatively frequent in comparison with Alloy A in which not a single SISF was observed, but this may be due to the activation of a secondary slip system as a result of the high strain in Alloy B. In addition, all SISFs observed had ordering consistent with what has been previously reported as LPT to χ phase which should have served to strengthen Alloy B as in LSHR [8, 10].

Also present are intersecting planar defects, which the present work will not analyze in great detail. Figure 9 shows an intersection in Alloy B, which contained a high density of these intersecting planar defects. Note that at the intersection point, these defects show enrichment of γ-formers Co and Cr (EDS not shown), as found in previous work by Barba et al.

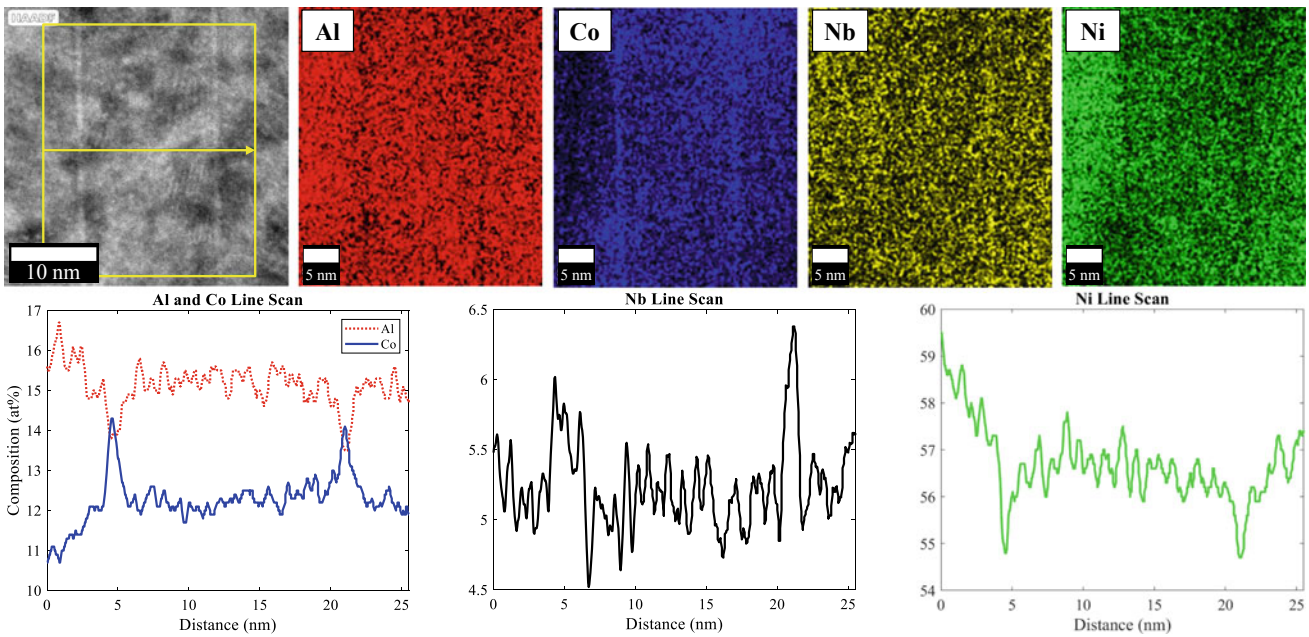

Fig. 6 HAADF image of Alloy B and accompanying EDS maps of segregating species. Vertically integrated EDS line scans across the twin as marked

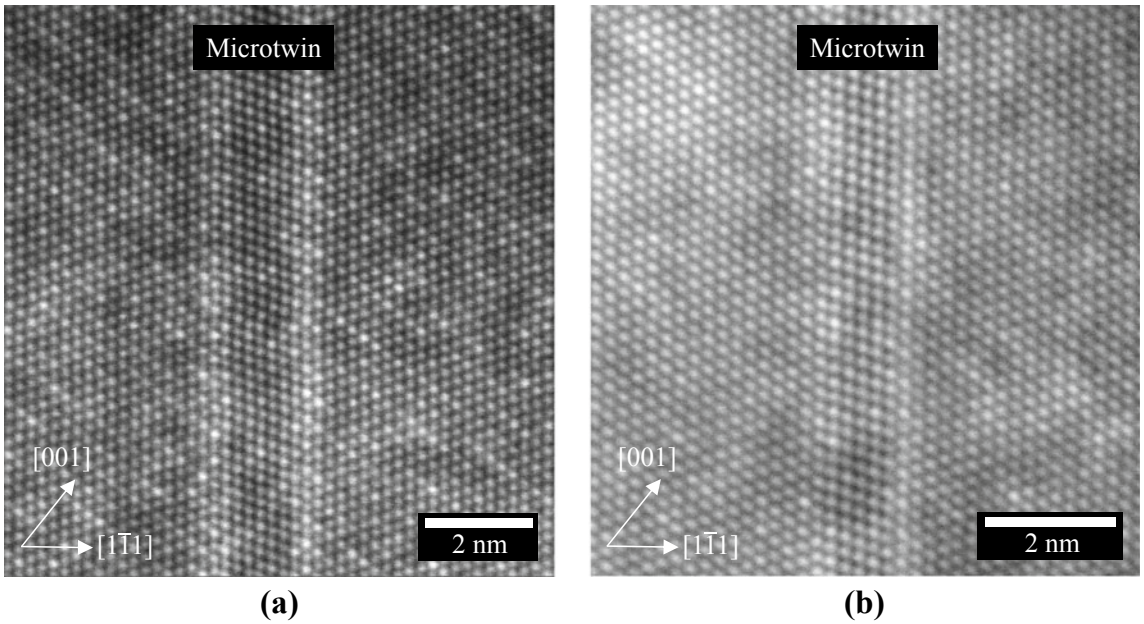

Fig. 7 Comparison of microtwin interfaces in alloys **a** A and **b** B

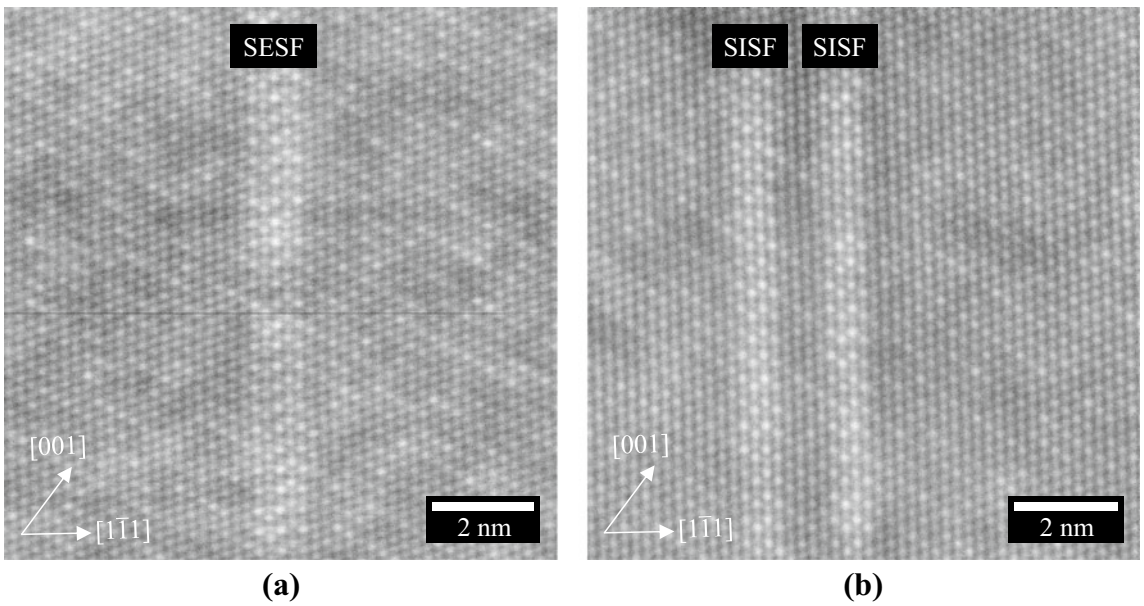

Fig. 8 **a** SESF with η LPT in Alloy A, and **b** two SISFs with χ LPT in Alloy B

[9]. The presence of these elements could help to reduce the energy penalty from increased atomic displacement, as in a Cottrell atmosphere leading partial dislocations, but may also relieve the stacking fault energy along the "pipe" that is formed as a result of the intersection defects.

The intersection in Alloy B is an interesting feature, as it shows both SESF and SISF, and a thin two-layer microtwin on the same slip system all impinging on a microtwin in a separate system. Given the thickness of the bottom microtwin, it is likely that this defect was the first to form and on the primary slip system. If the thick microtwin boundary is examined moving from right to left, it can be seen that it thickens following each intersecting event. In this case, one can imagine the leading partial dislocations of the impinging defects striking the microtwin boundary and proceeding to undergo a cross-slip event via transformation into a stair rod dislocation and a new partial dislocation that could then glide along the microtwin interface, thus

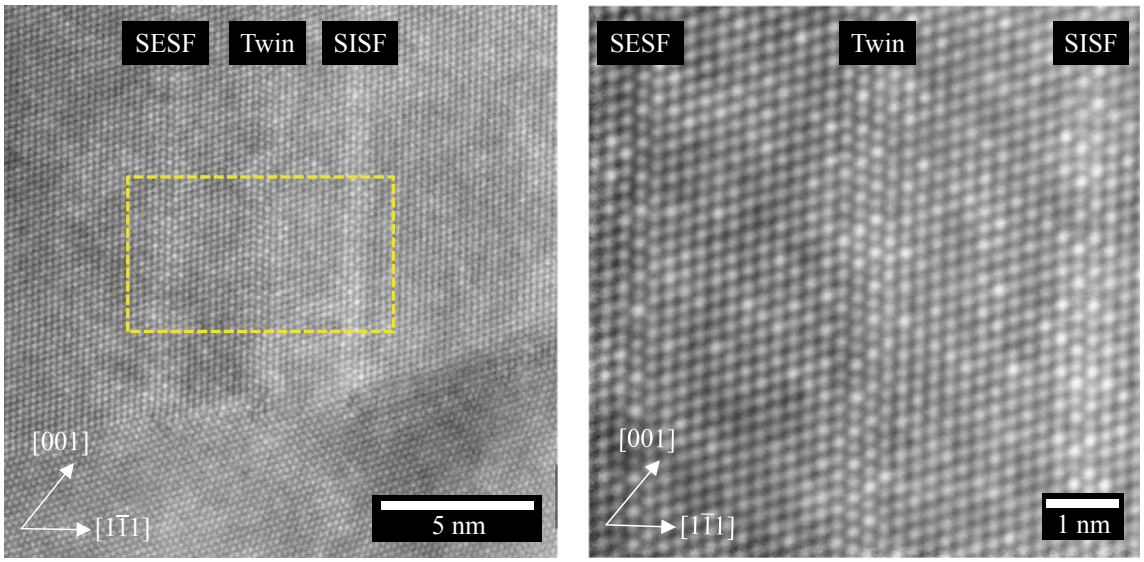

Fig. 9 **a** Impinging SESF, microtwin, and SISF on a thick microtwin in Alloy B. **b** Higher magnification image of the impinging planar defects

thickening it. In fact, the number of additional planes added to the thicker microtwin between the center, vertically oriented microtwin and the SESF on the left is four layers, exactly the number of Shockley partials required to create the two-layer thick microtwin.

Discussion

What is presently clear from the above analysis is that small changes in composition alone can have drastic effects on deformation response. This is seen in the remarkable creep strength in Alloy A, as compared to Alloy B (and others), caused by only a 1 at.% increase of Nb in the bulk composition. This has produced a novel LPT strengthening event along the microtwin boundary interfaces, which will now be examined in detail.

From previous works, it has been shown that LPT along planar defects, namely SESFs and SISFs, has caused significant improvement in creep performance versus those that instead exhibit segregation of γ forming elements [5, 8, 10, 11, 17]. This has been attributed to the presence of η preventing the thickening of SESFs to microtwins, and χ phases on SISFs inhibiting the propagation of stacking fault ribbons. In the case of Alloy A, it appears that LPT at the microtwin interface may act to halt the passage of thickening $a/6$ <112> partial dislocations which cause more rapid strain accumulation. This thickening is usually associated with the presence of both Co and Cr, the latter of which was not present in this alloy.

To determine the exact phase occurring in the LPT, the structure of the twin boundary interface was first examined. In the <110> viewing direction from which these planar defects are examined, it can be seen from inspection that a D0-type structure with a single unit cell in the <111> direction is formed from the two {111} planes inside the twin and the adjacent plane moving outside of the twin. This is additionally clarified in work by Bonnet et al. [25] in which microtwins could be examined alongside $D0_a$ δ phase in a γ'–δ heterointerface. While the presence of Nb at the appropriate sites could lead to the conclusion that this LPT is to the δ phase, one must take caution in this assumption. From this viewing direction alone, it cannot be confirmed in atomic resolution HAADF STEM what is occurring in the thickness of the foil. It is also possible that this could be $D0_{19}$ χ phase, as has previously been reported on SISFs [8, 10]. Both would share the same contrast effect and ordering pattern when viewed down <110> relative to γ', which is shown in Fig. 10. In order to determine which phase is present, we turn to density functional theory (DFT) to enlighten us on the energy landscape of the twin boundary interface.

The plane-wave-based density functional theory code VASP [26, 27] is used to calculate the energies of the two possible phases at the twin boundary. The ion-electron interactions are treated using pseudopotentials based on the projector-augmented wave method [28]. The exchange correlation is described by Perdew, Burke, and Ernzerhof [29] within the generalized gradient approximation scheme. The valence electron configurations are $3d^8 4s^2$, $3s^2 3p^1$, and

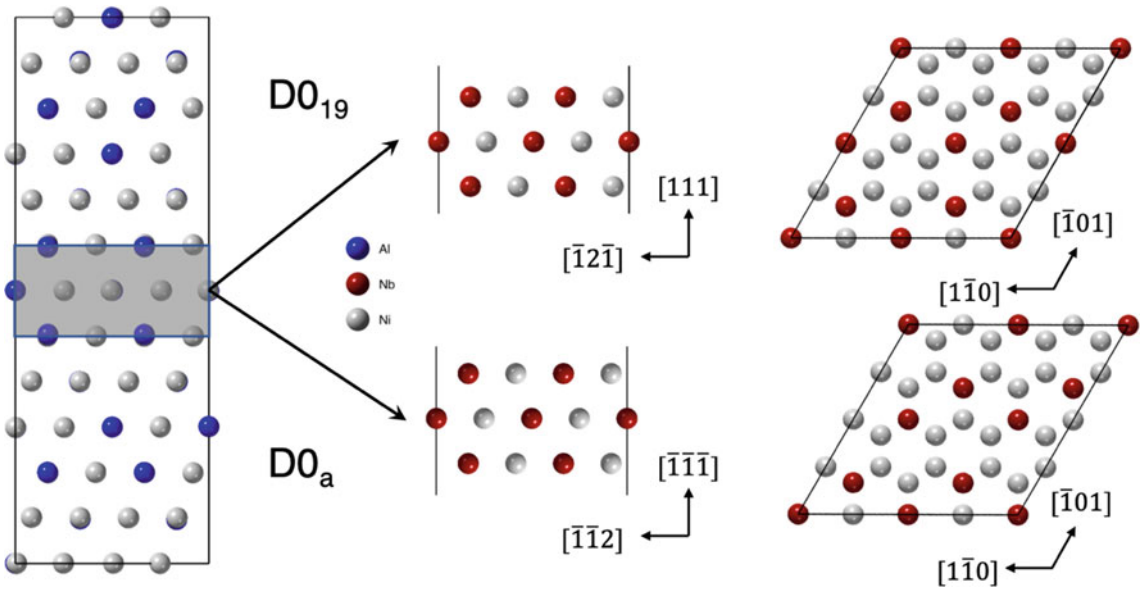

Fig. 10 Geometries used in the DFT simulations. The far left shows the simulation cell with a twin boundary. The shaded area will be replaced by either δ phase or χ phase. The χ phase has the $D0_{19}$ structure, whose configuration is shown in the top right. The δ phase has the $D0_a$ structure, which is shown in the bottom right

$5s^1 4d^4$ for Ni, Al, and Nb, respectively. A Monkhorst-Pack [30] k-point mesh of $3 \times 3 \times 1$ is used for the Brillouin zone integration. Relaxation of all degrees of freedom is allowed and the convergence criteria are 10^{-5} eV and 5×10^{-3} eV/Å for electronic and ionic steps, respectively. Spin-polarization is enabled in our calculations.

The simulation cell contains 192 atoms, consisting of 12 {111} layers. A twin boundary is introduced at the seventh layer by applying a burgers vector of $11\bar{2}/3$ on consecutive layers starting from the eighth layer. Then, the three layers at the twin boundary are replaced with a three-layer δ or χ phase. We only have Nb and Ni in these phases for simplification. Both phases are coherent with the γ' matrix. The only difference is the arrangement of those atoms, as shown in Fig. 10. Since the calculations involve the same number of atoms, these energies can be compared directly. Our results show that the energy for χ phase is −5.92 eV/atom, while for δ phase, it is −5.90 eV/atom. This suggests that a phase transformation to χ phase is more favorable.

Additionally, several authors studying Co-based superalloys have reported $D0_{19}$ χ phase as having composition rich in Nb (Co_3Nb) [31–35]. This expands on previous work [8, 10, 36] showing that the typical χ stoichiometry, Co_3W, can be expanded to include Mo. In the context of the LPT work, this means that W, Mo, and Nb may all be leveraged in superalloys to promote LPT strengthening via χ formation along SISFs, and now microtwins.

Note also that in the atomic resolution images of Alloy A, Fig. 7, the "zig-zag" appears to flip on either side of the microtwin. This is consistent in maintaining the geometry of the twin boundary and can easily be seen in the "chevron" created by the trace of the {100} atomic columns. Since the phase is present along both interfaces of the twin, this serves to prevent thickening from $a/6$ <112> partials of either sign on the same slip system. Additionally, thickening of microtwins via cross-slip events along their boundary, such as the case examined in Alloy B of impinging faults and microtwin, could be prevented by LPT of χ. This may lead to a further reduction in the degree of creep strain accumulated by such a phenomenon.

This discussion has focused on microtwins and χ LPT on their interfaces; as such, η LPT at SESFs has not been examined in detail here. Future work will explore if the formation of η phase serves as an additional strengthening mechanism. Evidence in Fig. 9 indicates lack of η LPT at the SESF, suggesting decrease in the formation of Alloy B. Additional study is needed to distinguish and quantify this effect between the Alloys A and B.

Conclusion

In this study, two alloys with slight differences in Nb content, A with higher Nb and B with lower Nb, were studied to elucidate the effect of subtle alloying additions on creep properties. Alloy A was found to possess superior creep strength, in terms of a lower creep strain rate, than Alloy B and also previously studied alloys ME3 and LSHR. Several conclusions may be drawn from this, which are here summarized:

1. A novel LPT strengthening effect has been discovered in Alloy A via atomic resolution HAADF STEM and EDS analysis. This has led to a significant creep strength increase, in terms of a lower creep strain rate, compared to an alloy that is deforming similarly excluding this effect.
2. The LPT is attributed to a 1 at.% increase in Nb content versus the comparable alloy without this phenomenon. Twin boundaries are segregated with significant Nb content, leading to the LPT, as opposed to typical γ-like segregation seen in Alloy B and in other Ni-based superalloys. It is clear that subtle alloying additions can have drastic effects on the high temperature creep strength in this alloy system.
3. DFT results suggest that this novel LPT strengthening phase is χ, which has been previously proposed as an LPT strengthening event on SISFs by preventing stacking fault ribbon formation.
4. Planar defects impinging onto already formed microtwins may undergo cross-slip events at the twin interface and proceed to thicken the twin. Formation of the novel χ LPT on microtwin boundaries may prevent this deleterious thickening from occurring.

The above conclusions serve to illustrate the need to determine "critical" solute concentrations in the γ' precipitates to reach the maximum strengthening potential in these alloys. Accurate determination of LPT phase space is paramount in improving current state of the art superalloys via LPT strengthening. This includes advanced computational techniques, such as Multi-Cell Monte Carlo (MC^2), as well as rapid exploration of compositions nearing bulk TCP formation.

Acknowledgments AJE and MJM acknowledge the support of the National Science Foundation and the DMREF program under Grant #1922239. TMS acknowledges NASA's Aeronautics Research Mission Directorate (ARMD)—Transformational Tools and Technologies Project and NASA's Advanced Air Transport Technology (AATT) Project Offices. ST gratefully acknowledges Rolls-Royce Corporation for provision of some of the alloys studied in this investigation. Electron microscopy was performed at the Center for Electron Microscopy and Analysis (CEMAS) at The Ohio State University.

References

1. Reed RC (2006) The Superalloys: Fundamentals and Applications. Cambridge University Press, New York.
2. Pollock TM, Tin S (2006) Nickel-Based Superalloys for Advanced Turbine Engines: Chemistry, Microstructure and Properties. J Propuls Power 22:361–374. https://doi.org/10.2514/1.18239.
3. Furrer D, Fecht H (1999) Ni-based Alloys for Turbine Discs. J Met 51:14–17.
4. Williams REA, Smith T, Esser BD, et al (2015) Super-X EDS Characterization of Chemical Segregation within a Superlattice Extrinsic Stacking Fault of a Ni-based Superalloy. Microsc Microanal 21:493–494. https://doi.org/10.1017/s1431927615003268.
5. Smith T, Esser B, Antolin N, et al (2016) Phase transformation strengthening of high-temperature superalloys. Nat Commun 7:1–7. https://doi.org/10.1038/ncomms13434.
6. Barba D, Alabort E, Pedrazzini S, et al (2017) On the microtwinning mechanism in a single crystal superalloy. Acta Mater 135:314–329. https://doi.org/10.1016/j.actamat.2017.05.072.
7. Smith TM, Rao Y, Wang Y, et al (2017) Diffusion processes during creep at intermediate temperatures in a Ni- based superalloy. Acta Mater 141:261–272. https://doi.org/10.1016/j.actamat.2017.09.027.
8. Smith T, Esser B, Good B, et al (2018) Segregation and Phase Transformations Along Superlattice Intrinsic Stacking Faults in Ni-Based Superalloys. Metall Mater Trans A 49:4186–4198. https://doi.org/10.1007/s11661-018-4701-5.
9. Barba D, Smith TM, Miao J, et al (2018) Segregation-Assisted Plasticity in Ni-Based Superalloys. Metall Mater Trans A 49:4173–4185. https://doi.org/10.1007/s11661-018-4567-6.
10. Smith TM, Good BS, Gabb TP, et al (2019) Effect of stacking fault segregation and local phase transformations on creep strength in Ni-base superalloys. Acta Mater 172:55–65. https://doi.org/10.1016/j.actamat.2019.04.038.
11. Smith T, Esser B, Antolin N, et al (2015) Segregation and eta phase formation along stacking faults during creep at intermediate temperatures in a Ni-based superalloy. Acta Mater 100:19–31. https://doi.org/10.1016/j.actamat.2015.08.053.
12. Smith TM, Unocic RR, Deutchman H, Mills MJ (2016) Creep deformation mechanism mapping in nickel base disk superalloys. Mater High Temp 33:372–383. https://doi.org/10.1080/09603409.2016.1180858.
13. Freund LP, Messe OMDM, Barnard JS, et al (2017) Segregation assisted microtwinning during creep of a polycrystalline L12-hardened Co-base superalloy. Acta Mater 123:295–304. https://doi.org/10.1016/j.actamat.2016.10.048.
14. Eggeler YM, Müller J, Titus MS, et al (2016) Planar defect formation in the γ' phase during high temperature creep in single crystal CoNi-base superalloys. Acta Mater 113:335–349. https://doi.org/10.1016/j.actamat.2016.03.077.
15. Makineni SK, Kumar A, Lenz M, et al (2018) On the diffusive phase transformation mechanism assisted by extended dislocations during creep of a single crystal CoNi-based superalloy. Acta Mater 155:362–371. https://doi.org/10.1016/j.actamat.2018.05.074.
16. Viswanathan GB, Shi R, Genc A, et al (2015) Segregation at stacking faults within the γ' phase of two Ni-base superalloys following intermediate temperature creep. Scr Mater 94:5–8. https://doi.org/10.1016/j.scriptamat.2014.06.032.
17. Titus MS, Rhein RK, Wells PB, et al (2016) Solute segregation and deviation from bulk thermodynamics at nanoscale crystalline defects. Sci Adv 2:1–7. https://doi.org/10.1126/sciadv.1601796.
18. Antonov S, Detrois M, Helmink RC, Tin S (2015) Precipitate phase stability and compositional dependence on alloying additions in γ-γ'-δ-η Ni-base superalloys. J Alloys Compd 626:76–86. https://doi.org/10.1016/j.jallcom.2014.11.155.
19. Viswanathan GB, Sarosi PM, Henry MF, et al (2005) Investigation of creep deformation mechanisms at intermediate temperatures in René 88 DT. Acta Mater 53:3041–3057. https://doi.org/10.1016/j.actamat.2005.03.017.
20. Karthikeyan S, Unocic RR, Sarosi PM, et al (2006) Modeling microtwinning during creep in Ni-based superalloys. Scr Mater 54:1157–1162. https://doi.org/10.1016/j.scriptamat.2005.11.049.

21. Viswanathan GB, Karthikeyan S, Sarosi PM, et al (2006) Microtwinning during intermediate temperature creep of polycrystalline Ni-based superalloys: mechanisms and modelling. Philos Mag 86:29–31. https://doi.org/10.1080/14786430600767750.
22. Sarosi PM, Viswanathan GB, Mills MJ (2006) Direct observation of an extended complex stacking fault in the gamma' phase of a Ni-base superalloy. Scr Mater 55:727–730. https://doi.org/10.1016/j.scriptamat.2006.06.019.
23. Kolbe M (2001) The high temperature decrease of the critical resolved shear stress in nickel-base superalloys. Mater Sci Eng A A319–321:383–387.
24. Kovarik L, Unocic RR, Li J, et al (2009) Microtwinning and other shearing mechanisms at intermediate temperatures in Ni-based superalloys. Prog Mater Sci 54:839–873. https://doi.org/10.1016/j.pmatsci.2009.03.010.
25. Bonnet R, Loubradou M, Dahmen U (2000) Atomic scale observation of the displacement fields generated by the intrinsic defects of {1 1 1}Ni 3 Al/(0 1 0)Ni 3 Nb close-packed interfaces. Philos Mag A 80:2233–2256.
26. Kresse G, Furthmüller J (1996) Efficient iterative schemes for *ab initio* total-energy calculations using a plane-wave basis set. Phys Rev B 54:11169–11186. https://doi.org/10.1103/physrevb.54.11169.
27. Kresse G, Joubert D (1999) From ultrasoft pseudopotentials to the projector augmented-wave method. Phys Rev B 59:1758–1775. https://doi.org/10.1103/physrevb.59.1758.
28. Blochl PE (1994) Projector augmented-wave method. Phys Rev B 50:17953–17979.
29. Perdew JP, Burke K, Ernzerhof M (1996) Generalized Gradient Approximation Made Simple. Phys Rev Lett 77:3865–3868.
30. Monkhorst HJ, Pack JD (1976) Special points for Brillonin-zone integrations*. Phys Rev B 13:5188–5192.
31. Makineni SK, Nithin B, Palanisamy D, Chattopadhyay K (2016) Phase evolution and crystallography of precipitates during decomposition of new "tungsten-free" Co(Ni)–Mo–Al–Nb γ–γ′ superalloys at elevated temperatures. J Mater Sci 51:7843–7860. https://doi.org/10.1007/s10853-016-0026-1.
32. Makineni SK, Nithin B, Chattopadhyay K (2015) A new tungsten-free γ-γ' Co-Al-Mo-Nb-based superalloy. Scr Mater 98:36–39. https://doi.org/10.1016/j.scriptamat.2014.11.009.
33. Makineni SK, Nithin B, Chattopadhyay K (2015) Synthesis of a new tungsten-free γ-γ′ Cobalt-based superalloy by tuning alloying additions. Acta Mater 85:85–94. https://doi.org/10.1016/j.actamat.2014.11.016.
34. Tomaszewska A, Mikuszewski T, Moskal G, Migas D (2018) Primary microstructure, microsegregation and precipitates characterization of an as-cast new type γ-γ′ Co-Al-Mo-Nb cobalt-based superalloy. J Alloys Compd 750:741–749. https://doi.org/10.1016/j.jallcom.2018.03.397.
35. Tirado FLR, Toinin JP, Dunand DC (2018) γ + γ′ microstructures in the Co-Ta-V and Co-Nb-V ternary systems. Acta Mater 151:137–148. https://doi.org/10.1016/j.actamat.2018.03.057.
36. Meher S, Banerjee R (2014) Partitioning and site occupancy of Ta and Mo in Co-base γ/γ′ alloys studied by atom probe tomography. Intermetallics 49:138–142. https://doi.org/10.1016/j.intermet.2014.01.020.